

Moiré band structure engineering using a twisted boron nitride substrate

Received: 12 November 2024

Accepted: 11 December 2024

Published online: 02 January 2025



Xirui Wang¹, Cheng Xu², Samuel Aronson¹, Daniel Bennett³, Nisarga Paul^{1,4}, Philip J. D. Crowley⁵, Clément Collignon¹, Kenji Watanabe⁶, Takashi Taniguchi⁷, Raymond Ashoori¹, Efthimios Kaxiras^{3,5}, Yang Zhang^{2,8}, Pablo Jarillo-Herrero¹✉ & Kenji Yasuda^{1,9}✉

Applying long wavelength periodic potentials on quantum materials has recently been demonstrated to be a promising pathway for engineering novel quantum phases of matter. Here, we utilize twisted bilayer boron nitride (BN) as a moiré substrate for band structure engineering. Small-angle-twisted bilayer BN is endowed with periodically arranged up and down polar domains, which imprints a periodic electrostatic potential on a target two-dimensional (2D) material placed on top. As a proof of concept, we use Bernal bilayer graphene as the target material. The resulting modulation of the band structure appears as superlattice resistance peaks, tunable by varying the twist angle, and Hofstadter butterfly physics under a magnetic field. Additionally, we demonstrate the tunability of the moiré potential by altering the dielectric thickness underneath the twisted BN. Finally, we find that near-60°-twisted bilayer BN also leads to moiré band features in bilayer graphene, which may come from the in-plane piezoelectric effect or out-of-plane corrugation effect. Tunable twisted BN substrate may serve as versatile platforms to engineer the electronic, optical, and mechanical properties of 2D materials and van der Waals heterostructures.

The emerging concept of quantum metamaterials enables us to engineer electronic structures and physical properties that do not exist in natural crystals¹. This is most strikingly exemplified by moiré materials, where two-dimensional (2D) materials are stacked at controlled angles. For instance, twisted bilayer graphene and transition metal dichalcogenide moiré bilayers exhibit topological and strongly-correlated phases of matter, absent in their constituent layers^{2–11}. Despite the prosperous findings in these moiré systems, the method of creating a moiré potential by twisting the target material itself poses limitations

in the choice of materials, moiré periodicity, and potential strength. This is mainly due to the requirement of the proximity of two atomic layers with similar or identical lattice constants.

A remote tunable superlattice potential isolated from a target layer can overcome these constraints. Past research has etched periodic holes in gate dielectrics or gate electrodes via electron beam lithography or focused ion beam milling, and introduced an electrostatic periodic potential in the target layers via gating^{12–18}. The effect of a periodic potential on graphene was observed as superlattice

¹Department of Physics, Massachusetts Institute of Technology, Cambridge, MA, USA. ²Department of Physics and Astronomy, University of Tennessee, Knoxville, TN, USA. ³John A. Paulson School of Engineering and Applied Sciences, Harvard University, Cambridge, MA, USA. ⁴Kavli Institute of Theoretical Physics, University of California, Santa Barbara, Santa Barbara, CA, USA. ⁵Department of Physics, Harvard University, Cambridge, MA, USA. ⁶Research Center for Electronic and Optical Materials, National Institute for Materials Science, 1-1 Namiki, Tsukuba, Japan. ⁷Research Center for Materials Nanoarchitectonics, National Institute for Materials Science, 1-1 Namiki, Tsukuba, Japan. ⁸Min H. Kao Department of Electrical Engineering and Computer Science, University of Tennessee, Knoxville, TN, USA. ⁹School of Applied and Engineering Physics, Cornell University, Ithaca, NY, USA. ✉e-mail: pjarillo@mit.edu; kenji.yasuda@cornell.edu

resistance peaks due to band folding and Hofstadter physics^{14–18}. Despite the versatility in shape and the tunability in the potential strength, this method suffers from two limitations. First, the pitch resolution is technically restricted when the pattern is defined by electron beam lithography or focused ion milling, being difficult to achieve below 16 nm¹⁷, because of the secondary electrons or limitation in beam size. Second, as each pitch is written independently through lithography or focused ion beam, the unavoidable non-identity among moiré sites works as disorder in the moiré potential, leading to broadened superlattice peaks and potentially smearing out detailed features. A natural way to overcome this issue is to create moiré potentials via twisted van der Waals (vdW) materials, which can achieve arbitrary moiré periodicity by controlling the twist angle, and highly periodic moiré superlattices formed from identical unit cells due to their crystalline nature^{19–21}.

We engineer such a moiré substrate using a twisted 2D insulator – twisted bilayer boron nitride (BN). Hexagonal BN is one of the most important constituents of vdW heterostructures, which is primarily used as an atomically-flat substrate and gate dielectric. Recently, it has been demonstrated that out-of-plane ferroelectricity can be obtained by stacking two monolayers of BN in parallel^{22–24}. Furthermore, a moiré polar pattern is generated by introducing a small angle between the monolayers (Fig. 1b), which is characterized by upward and downward polarizations periodically arranged in the lateral direction^{22–25}. Using twisted bilayer BN as a substrate, we can apply a moiré electrostatic potential to arbitrary 2D materials²⁶. Here, we use bilayer graphene as the target material, illustrating the resultant band structure modification and the tunability of the twisted BN moiré substrates.

A monolayer BN consists of boron (B) and nitrogen (N) atoms alternately arranged at honeycomb lattice sites. When two BN monolayers are twisted at a small angle away from parallel stacking, a moiré pattern consisting of AA, AB, and BA stacking regions is formed as

illustrated in Fig. 1b. In AA stacking, the top and bottom layers directly overlap, having no net polarization. In AB (BA) stacking, meanwhile, B (N) sits on top of the N (B) atom, forming an electric dipole and giving rise to downward (upward) polarization (Fig. 1a)^{23,24}. We consider such twisted bilayer BN as forming a moiré polar substrate, referring to the fact that the moiré potential comes from the electrostatic potential in these staggered up and down polar domains. Figure 1c illustrates the schematic of our device, where we placed a target layer on top of the twisted BN moiré substrate, controlled with a top metal gate and a bottom graphite gate. In this device geometry, we expect the modulation of the potential U on the target layer yielding a peak magnitude of around 29 mV when the moiré wavelength is 18.5 nm, and the target layer is bilayer graphene (Fig. 1d, see simulation details in Methods). Figure 1e displays the theoretical calculation of the band structure. The superlattice moiré potential leads to the band folding into a mini-Brillouin zone, with density of state (DOS) minima at the band edges (see calculation details in Supplementary Note 1).

Results

Band structure modulation in bilayer graphene

We fabricated a series of bilayer graphene/twisted bilayer BN devices (A1–A5), aiming at different twist angles between 0.4° and 1.3°. We first made the top stack by sequentially picking up the top BN, bilayer graphene, and twisted bilayer BN using the tear-and-stack technique. We intentionally misaligned the bilayer graphene with top and bottom BN layers to avoid the formation of long-periodicity moiré patterns by the BN to graphene alignment. Subsequently, we performed piezoresponse force microscopy (PFM) to identify regions with uniform moiré patterns. Finally, we placed the top stack onto the bottom graphite, etched and contacted the device. The detailed parameters of the devices are summarized in Supplementary Table 1, and the optical microscope images are shown in Supplementary Fig. 2. For transport measurements of devices A1–A5, we

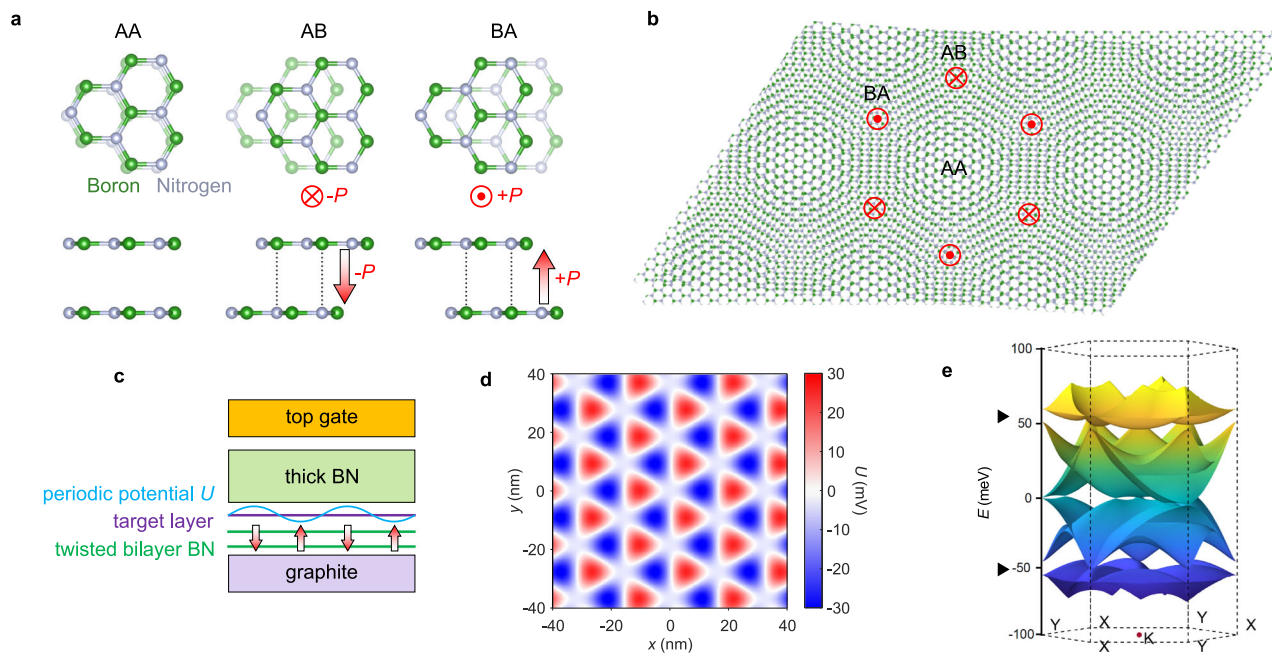


Fig. 1 | Twisted bilayer BN as a moiré polar substrate. **a** Three high-symmetry stacking orders that exist in near-0°-twisted bilayer BN⁶⁵. N and B atoms are shown in silver and green, respectively. In AA stacking (left), top and bottom atoms align right on top of each other, and there is no out-of-plane polarization. In AB (middle) and BA (right) stacking, the vertical alignment of N and B atoms creates an out-of-plane electric dipole, leading to downward (upward) polarization in AB (BA) stacking. **b** Schematic of twisted bilayer BN, where moiré patterns form with AB (downward polarization), BA (upward polarization), and AA local stacking arrangements⁶⁵. **c** Device schematic for using twisted BN as a moiré polar substrate.

Target layer sits on top of twisted bilayer BN, feeling its periodic moiré potential U . The target layer is encapsulated by a thick BN on top, and electrically gated with a metal top gate and a graphite bottom gate. **d** Electrostatic simulation of potential strength U imposed on bilayer graphene in the device structure shown in **c**, and the moiré wavelength a is taken to be 18.5 nm. **e** Band structure calculation of bilayer graphene under the electrostatic moiré potential in **(d)**. Arrows mark the locations of density of state (DOS) minima in the conduction band and valence band due to band folding induced by the superlattice potential.

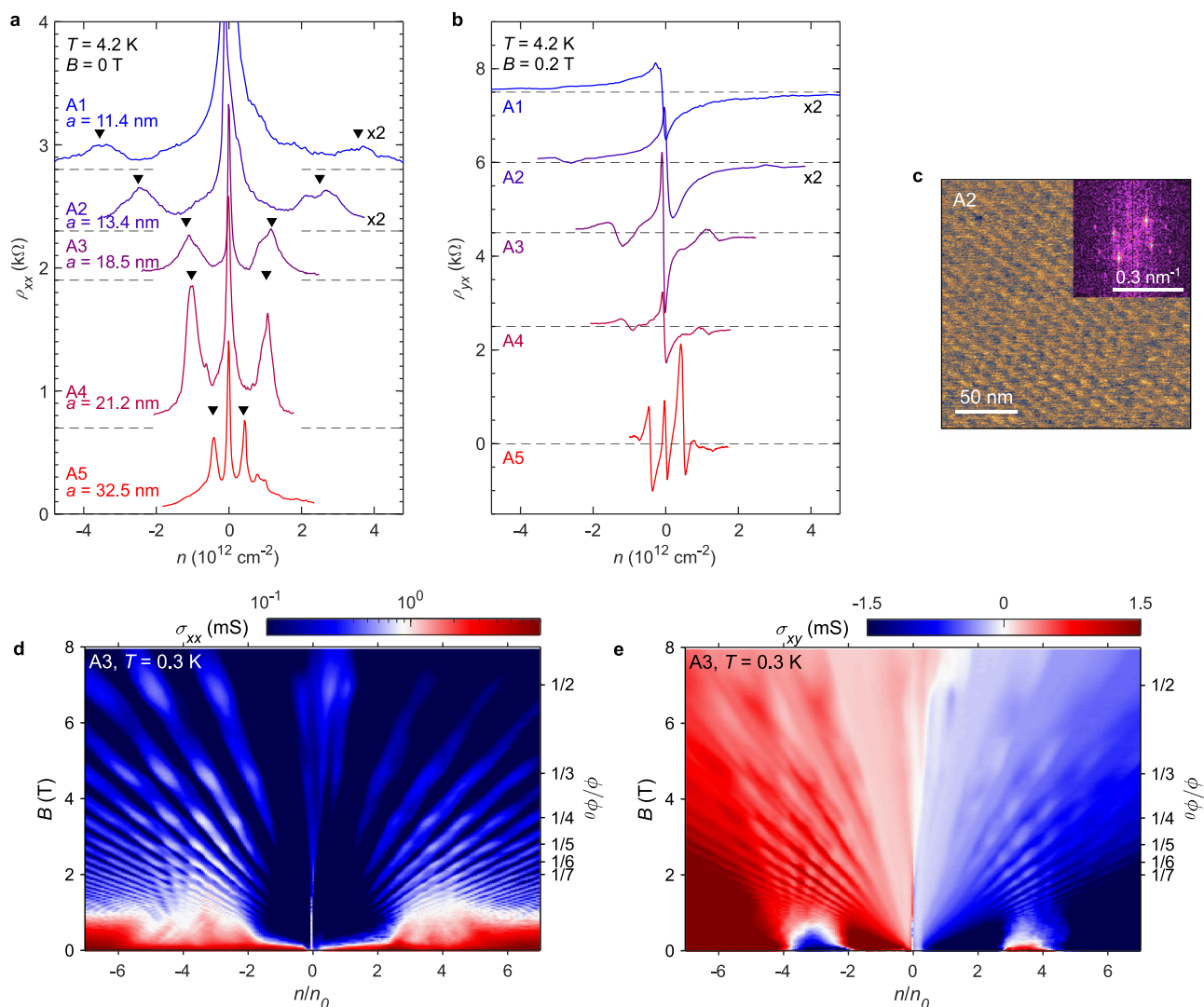


Fig. 2 | Band structure modulation of bilayer graphene on twisted bilayer BN moiré polar substrate. **a** Longitudinal resistivity ρ_{xx} as a function of carrier density n in devices A1–A5, measured at 4.2 K. Satellite resistance peaks symmetrically located around CNP are observed at different carrier densities that correspond to different moiré wavelengths. Arrows indicate the positions of the satellite resistance peaks. **b** Hall resistivity ρ_{yx} as a function of n in devices A1–A5 at $B = 0.2$ T, $T = 4.2$ K. **c** Piezoresponse force microscopy (PFM) image of twisted BN before

making into device A2. Scale bar: 50 nm. Inset: Fourier transform image. Scale bar: 0.3 nm^{-1} . **d** Longitudinal conductance σ_{xx} as a function of filling factor n/n_0 and magnetic field B (right y axis: normalized magnetic flux ϕ/ϕ_0), measured at 0.3 K in device A3. $\phi = BA$, the magnetic flux per moiré unit cell, and flux quantum $\phi_0 = h/e$. **e** Transverse conductance σ_{xy} as a function of n/n_0 and B (right y axis: ϕ/ϕ_0), measured at 0.3 K in device A3.

grounded both the bilayer graphene and bottom graphite to prevent tunneling or capacitive coupling between them. Figure 2a plots the longitudinal sheet resistivity ρ_{xx} as a function of carrier density n , calibrated from Landau fan diagram measurements. We observe satellite resistance peaks symmetrically located around the charge neutrality point (CNP) at different carrier densities for A1–A5. According to the band structure calculation in Fig. 1e, we expect DOS minima, *i.e.*, resistance peaks, at the filling of one moiré band on both the electron and hole sides, corresponding to $n_0 = 4/A$, where $A = \sqrt{3}/2 a^2$ is the moiré unit cell area, and the prefactor 4 corresponds to the spin and valley degeneracy. The moiré wavelength of device A2 calculated from the satellite resistance peak positions is around 13.4 nm, which is consistent with the one obtained from the PFM image, 11.9 nm (Fig. 2c). This agreement confirms that the satellite resistance peaks originate from the band structure modulation induced by the twisted BN moiré substrate. Additional PFM images are included in Supplementary Fig. 3.

Our method can produce arbitrary moiré periodicity by tuning the twist angle, which is in contrast to the moiré periodicity formed by BN to graphene alignment. The latter cannot be longer than 14 nm

because of the finite lattice mismatch. We also note that when the moiré potential was induced by aligning a piece of BN to graphene, the hole side typically featured a more prominent resistance peak than the electron side^{27–29}, while in our devices, the heights of resistance peaks on both sides are comparable, in line with the symmetric DOS minima on the electron and hole sides in Fig. 1e and Supplementary Fig. 1. We speculate that the variations in the satellite resistance peak widths come from the twist angle disorder in our devices (see discussions in Supplementary Note 3).

The Hall resistivity ρ_{yx} under a small magnetic field ($B = 0.2$ T) as a function of n shows sign reversals at the satellite resistance peak positions as well as between CNP and satellite resistance peak positions (Fig. 2b). The former can be attributed to the moiré band edges, and the latter to the Van Hove singularities (VHSs). We note that both the satellite resistance peaks in ρ_{xx} and sign reversals in ρ_{yx} become stronger when the moiré wavelength increases. We can qualitatively understand this trend as the following: since the wavevector is inversely proportional to the moiré wavelength, as the moiré wavelength increases, the kinetic energy at the mini-Brillouin zone boundary

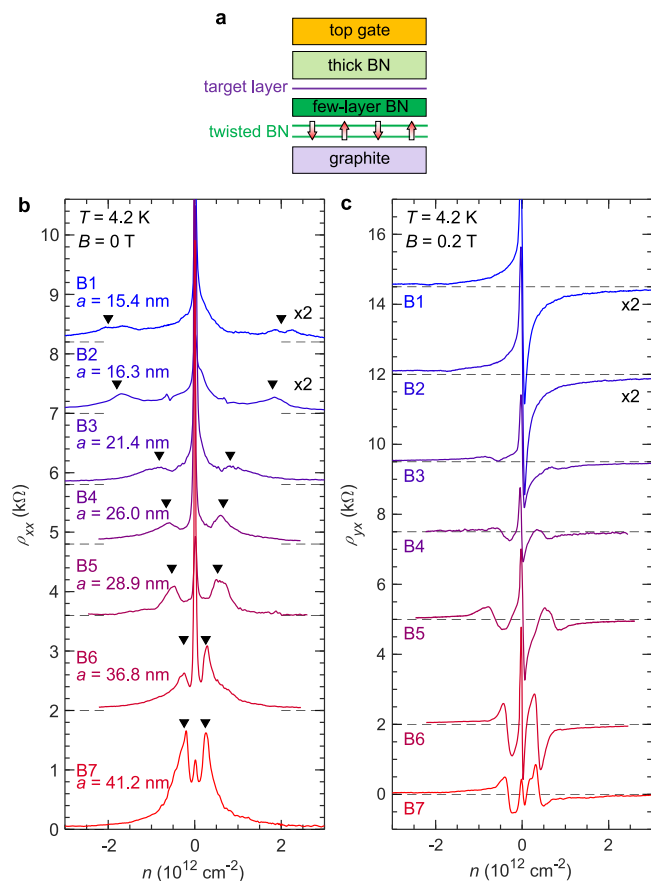


Fig. 3 | Devices with inserted BN above near-0°-twisted bilayer BN. a Schematic of devices with inserted BN between twisted bilayer BN and bilayer graphene. **b** ρ_{xx} as a function of n in devices B1-B7 measured at 4.2 K. **c** ρ_{xx} as a function of n in devices B1-B7 at 4.2 K, $B = 0.2$ T.

decreases. Therefore, the relative effect of the electrostatic potential is enhanced, leading to a stronger band reconstruction (see discussions in Supplementary Note 4).

We further investigate the magnetic field response by increasing the magnetic field and plotting the longitudinal conductance σ_{xx} versus filling factor n/n_0 and the normalized magnetic flux ϕ/ϕ_0 in Fig. 2d. We observe Landau fan features emanating from $n/n_0 = +4$ and -4 , respectively, indicating the formation of moiré mini bands^{27–29}. We also observe Brown-Zak oscillations, corresponding to enhanced conductivity when the cyclotron orbits are commensurate with the moiré wavelengths at $\phi/\phi_0 = 1/2, 1/3, 1/4$, and so on³⁰. In the Landau fan diagram of transverse conductance σ_{xy} , the sign reversals diminish at a critical field of around 0.7 T on the hole side and 0.3 T on the electron side due to the magnetic breakdown (Fig. 2e, see data of other devices in Supplementary Fig. 6), where the electron motion deviates from the orbits determined by moiré band structure in our previous calculation in Fig. 1e. The difference in the critical magnetic fields points to the electron-hole asymmetry in the system. We can estimate the strength of the moiré potential based on the VHS location, which is expected to happen at a smaller filling factor as the moiré potential becomes larger (see calculation details in Supplementary Note 1). From the VHS location of $n/n_0 \approx -1.9$ on the hole side, we quantify the peak potential magnitude to be 105 mV, which is of the same order of magnitude as (albeit bigger than) our simulated moiré potential strength. As shown in the temperature dependence in Supplementary Fig. 7, the satellite resistance peaks persist up to 100 K, which is consistent with the moiré potential energy scale. Our transport measurements, together with PFM characterization and theoretical calculations, demonstrate that

twisted bilayer BN can work as a substrate to engineer moiré superlattices with different wavelengths and induce band structure modifications to 2D materials. The satellite resistance peaks, and the sign reversals of the Hall resistance are also observable in monolayer graphene on twisted BN (Supplementary Fig. 8), demonstrating the versatility of our moiré band engineering method.

Besides the moiré electrostatic effect, the structural lattice deformation effect has also been considered important in moiré heterostructures and band structure modulation^{20,31–39}. To verify the dominating role of electrostatic effect in band structure modulation of the target layer, we fabricated devices with inserted few-layer BN between bilayer graphene and twisted BN, in order to suppress the structural effect while maintaining the electrostatic effect (Fig. 3a). As shown in Fig. 3b, c, we observed clear satellite resistance peaks and Hall sign reversals in devices B1-B7. The strength of these moiré band features is comparable to devices A1-A5, showing that electrostatic effect plays a leading role here in band structure engineering.

Tuning moiré potential by inserting extra dielectric BN

Next, we demonstrate the tunability of the strength of the moiré potential by inserting extra dielectric BN underneath the twisted bilayer BN. When a thick BN is inserted between the bottom gate and a ferroelectric bilayer BN (in this paper, “thick BN” stands for 5 to 80 nm), the doping induced in the target layer is suppressed due to the larger distance between the target layer and the gate electrode²³. In Fig. 4a, we simulated the superlattice potential induced by the twisted bilayer BN at different total bottom BN thicknesses, denoted as d . The peak potential U_{peak} is plotted as a function of d , decreasing from 29 mV in the case without bottom thick BN to 11 mV at $d \geq 10$ nm (see simulation details in Supplementary Note 7). Figure 4b presents a comparison between two devices with a similar moiré wavelength: device A3 without bottom thick BN and device C1 with bottom thick BN ($d = 15.1$ nm). The heights of satellite resistance peaks in device C1 are less than one third of those in device A3, consistent with the smaller magnitude of the moiré potential.

As the magnetic field is turned on, we observe a similar yet weaker Hofstadter spectrum in device C1, with Landau levels emerging from moiré band edges, as well as Brown-Zak oscillations (Fig. 4c). The sign reversals in σ_{xy} diminish at around 0.3 T on the hole side, and no sign reversal is observed on the electron side except for a weakly reduced Hall conductance (Fig. 4d). The VHS is located at $n/n_0 \approx -3.0$ on the hole side, from which we extracted the peak potential to be 41 mV, around 40% of the value we extracted in device A3. The shifts in VHS locations, the lower satellite peak heights, weaker Hofstadter spectrum, and smaller critical field of Hall sign reversals, are all consistent with the weaker moiré potential in device C1 as compared to device A3. Additional data of more devices with inserted thick bottom BN are shown in Supplementary Figs. 10 and 11.

Moiré effect from near-60°-twisted BN

So far, we have only considered the electrostatic effect from the polar domains in the twisted bilayer BN. However, multifaceted moiré physics exist in our system besides the ferroelectric charge transfer, such as corrugation, lattice relaxation, interlayer hybridization and piezoelectric effect⁴⁰. Using near-60°-twisted BN, we demonstrate that effects other than the polar domain effect can also give rise to band folding and moiré physics in the target layer.

Different from the near-0°-twisted case, near-60°-twisted bilayer BN consists of AA', AB', and BA' stacking arrangements (Fig. 5b). Here, ' means one layer is rotated by 60° with respect to the other. The AA' stacking has each B atom stacked on top of an N atom or vice versa, and the AB' (BA') stacking has N (B) stacked on top of N (B) atoms (Fig. 5a). Importantly, all of these stacking orders have an inversion center, i.e., the top and bottom layers are connected by the inversion operation. This also holds true for low-symmetry stacking orders other

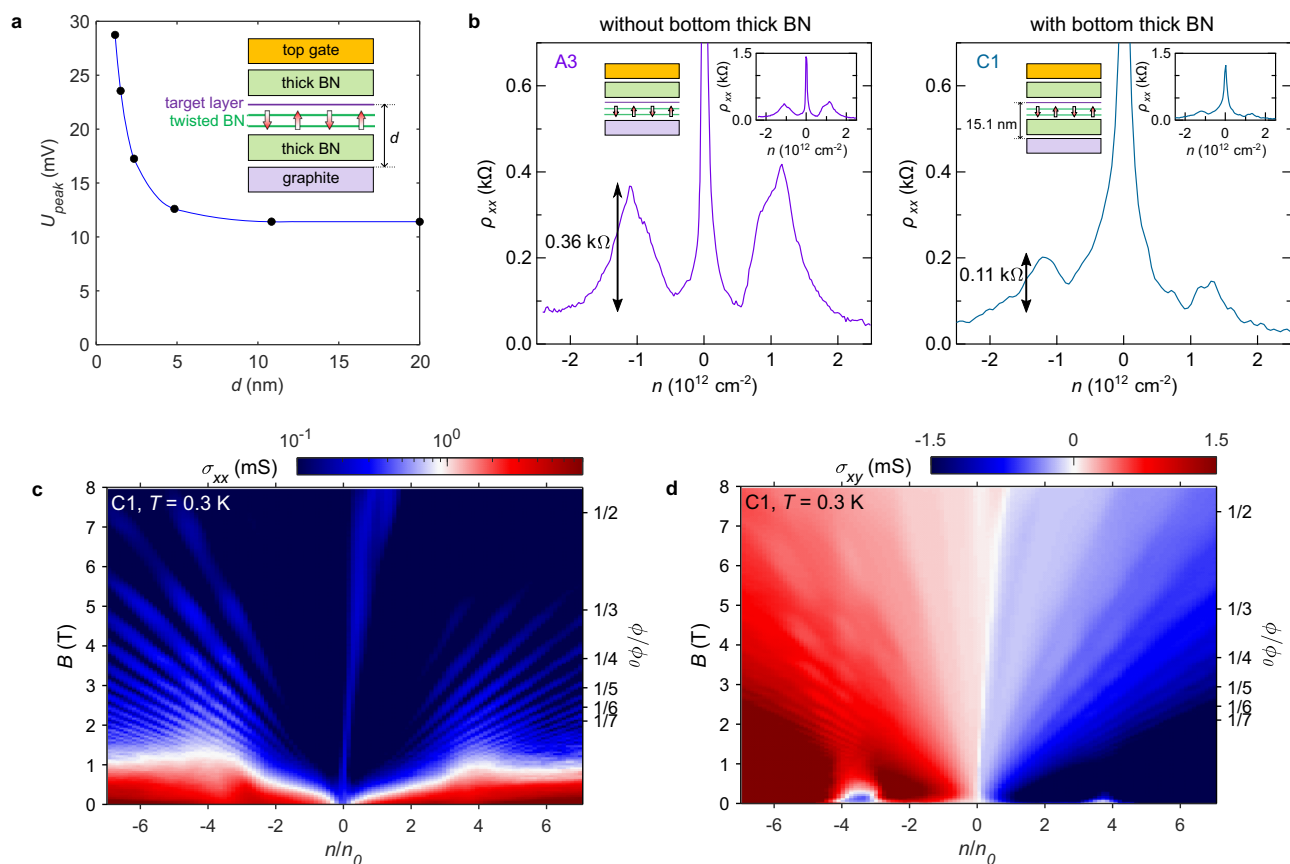


Fig. 4 | Tuning moiré polar potential by changing dielectric thickness.

a Electrostatic simulation of the moiré potential peak magnitude U_{peak} as a function of total bottom BN thickness d . Inset: Device schematic. A thick BN layer is inserted between the twisted bilayer BN and the bottom graphite. **b** ρ_{xx} as a function of n in

devices A3 (without bottom thick BN) and C1 (with bottom thick BN), measured at 4.2 K. Insets: Device schematics (left) and large-scale plots (right). **c** σ_{xx} as a function of n/n_0 and B (right y axis: ϕ/ϕ_0), measured at 0.3 K in device C1. **d** σ_{xy} as a function of n/n_0 and B (right y axis: ϕ/ϕ_0), measured at 0.3 K in device C1.

than AA', AB', and BA'. Hence, the polar domains and associated electrostatic potential are absent in near-60°-twisted BN (Fig. 5a). We prepared a device consisting of a bilayer graphene on top of a 60.90°-twisted bilayer BN, encapsulated by top and bottom thick BNs (Fig. 5c). We observed small satellite resistance peaks in ρ_{xx} plotted as a function of n , corresponding to the full filling of the moiré unit cell (Fig. 5d, e). Additional data from devices with near-60°-twisted BN are included in Supplementary Figs. 11 and 12.

We propose two possible mechanisms of the moiré band modulation by the near-60°-twisted BN – in-plane piezoelectric effect and out-of-plane corrugation effect. The moiré lattice relaxation in twisted BN causes in-plane strain, leading to in-plane charge redistribution through the piezoelectric effect⁴⁰. This can modulate the charge distribution periodically in the adjacent bilayer graphene. Meanwhile, the interlayer distance (d_0) between the two monolayers of BN varies depending on the stacking order, with spatial modulation as large as 7% according to the density functional theory (DFT) calculations (Fig. 5f, see calculation details in Supplementary Note 9). This out-of-plane corrugation may imprint partially into the interlayer distance of bilayer graphene, modulating the interlayer tunneling strength by the moiré periodicity and giving rise to band folding. The strength of the piezoelectric effect and corrugation effect depend on the twist angle, and their quantitative contributions are still under explore, which calls for future experimental and theoretical studies to uncover the rich moiré physics from twisted BN system^{31,40}.

Discussion

In conclusion, we demonstrated that twisted bilayer BN can serve as a versatile moiré substrate for band structure engineering with tunable

moiré wavelength and potential strength. With a well-defined potential landscape from polar domains, twisted BN hosts advantage for engineering the band structure of a wide range of 2D materials^{41,42} compared with moiré potential formed by doped electrons in moiré superlattices^{19–21,43}.

Our moiré polar substrate design principle is applicable not only to BN, but also to other bipartite 2D insulators or semiconductors, such as transition metal dichalcogenides, which have different magnitudes of electrostatic potential and spin-orbit interaction^{44,45}. The application of the moiré substrates on various 2D materials may lead to the observation of exotic physics related to correlations and topology in the future^{26,46–59}. Moreover, this lithographically free method for introducing highly periodic electrostatic potentials at the nanoscale may find applications in other fields of nanotechnology beyond 2D materials^{60–62}.

Methods

Device fabrication

BN and graphite crystals were exfoliated onto SiO₂ (285 nm–295 nm)/Si substrates. For monolayer BN, we used SiO₂ (90 nm)/Si substrates. The thickness of thick BN flakes (>5 nm) was acquired by atomic force microscopy (AFM). Monolayer BN, graphene and bilayer graphene were identified by optical contrast. We first prepared the bottom stacks. For devices A1–A6, B1–B7 we exfoliated graphite for bottom gates on SiO₂ (285 nm)/Si substrates with pre-patterned markers, followed by heat cleaning in an atmosphere of Ar (40 sccm) and H₂ (20 sccm) gases at 350 °C for more than 12 hours to remove the tape residues. For devices C1–C5, D1, and D2, a thick BN (5–20 nm) and graphite were sequentially picked up by poly(bisphenol A carbonate) (PC)-film-covered Polydimethylsiloxane (PDMS) stamp on a glass slide, and then released to a

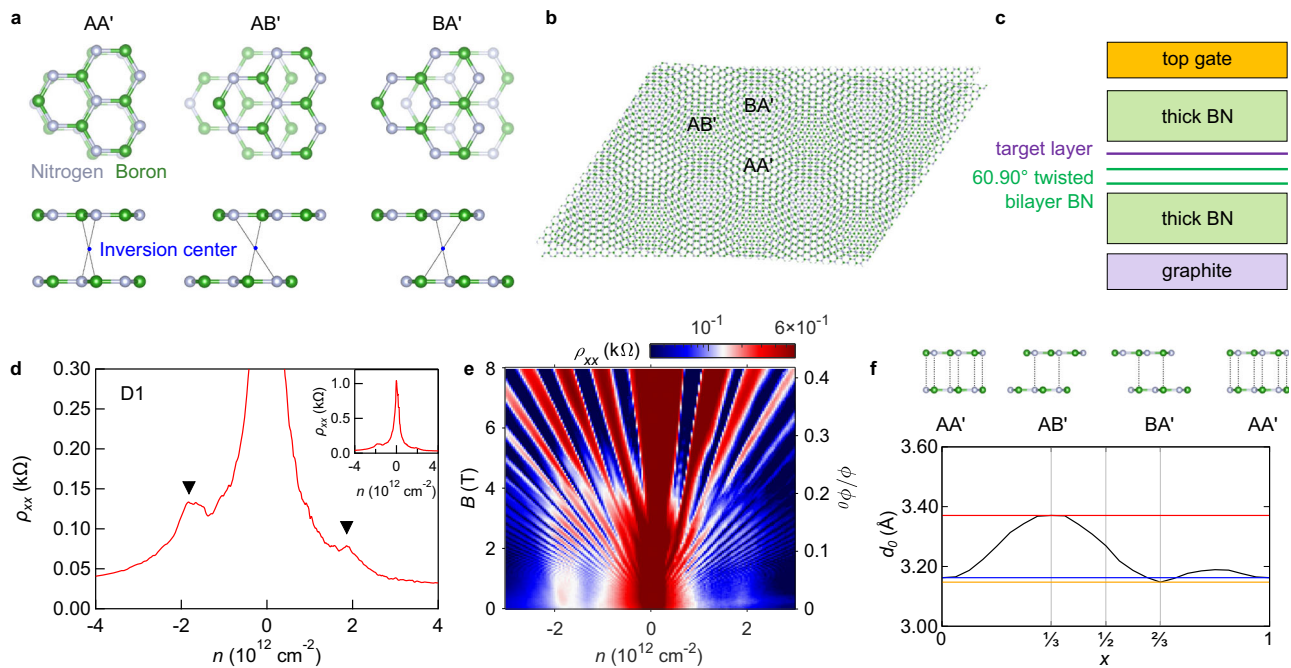


Fig. 5 | Moiré potential in near-60°-twisted bilayer BN. **a** Three stacking orders that exist in near-60°-twisted bilayer BN⁶⁵. In AA' stacking (left), B and N atoms align on top of each other alternatively. Here, ' means one layer is rotated by 60° with respect to the other. In AB' stacking (middle), N sits on top of N. In BA' stacking (right), B sits on top of B. All of these stacking arrangements have an inversion center, and therefore no net polarization is allowed. **b** Schematic of near-60°-twisted bilayer BN, where moiré patterns form with AA', AB', and BA' local stacking arrangements. **c** Device schematic of D1. The target layer sits on top of a near-60°-

twisted bilayer BN. The stack is encapsulated between the top and bottom BN and controlled by a top metal gate and a bottom graphite gate. **d** ρ_{xx} as a function of n in device D1 with near-60°-twisted bilayer BN, measured at 4.2 K. Arrows indicate the positions of the satellite resistance peaks. Inset: Large-scale plot. **e** ρ_{xx} as a function of n and B (right y axis: ϕ/ϕ_0), measured at 0.3 K in device D1. **f** Density functional theory (DFT) calculation of the interlayer distance d_0 between the two near-60°-twisted monolayer BNs at different moiré sites. x : fractions of the moiré unit cell.

SiO₂/Si substrate at 170 °C. We removed the trapped bubbles by moving the PC stamp and the stack up and down slowly a few times at 170 °C. After the PC was dissolved, the bottom stacks were heat cleaned in an atmosphere of Ar (40 sccm) and H₂ (20 sccm) gases at 350 °C for 3–12 hours. After that, contact mode AFM was performed at a deflection voltage of 0.1–0.2 V for cleaning the PC residues.

Each top stack was made by the sequential pickup of top BN, bilayer/monolayer graphene, (few-layer BN) and twisted bilayer BN. Twisted bilayer BN was obtained by the sequential pickup of monolayer BN flake at room temperature with the tear-and-stack method described in refs. 63,64. Then the stack on PC was scanned by PFM to search for regions with periodic moiré patterns. The whole stack was then released to the bottom graphite or bottom BN/graphite stack at 170 °C. The stack was identified with an optical microscope and AFM for bubble-free regions. Then the stack was etched into a Hall bar shape by reactive ion etching, leaving the bubble-free regions with periodic moiré patterns remained. All the contacts and top gates were deposited with Cr/Au with a thermal evaporator.

Piezoresponse force microscopy measurements

We performed lateral PFM measurements on the top stack containing twisted bilayer BN. The PFM measurements were performed with Asylum Research Cypher S atomic force microscope at room temperature. We used AC240TM-R3 tip with a force constant of around 1.5 N m⁻¹ and a contact resonance frequency of around 600 kHz with the applied AC bias voltage of 2 V. The contact strength was set to be lower than 30 nN to avoid unintentional damage to the flake and twist angle relaxation.

Transport measurements

The devices were bonded by aluminum wire. The four-probe measurements were done using lock-in amplifiers (SRS: SR830 and SR860), a current preamplifier (DL: Model 1211) and voltage preamplifiers (SRS:

SR560) at the frequency of 17–35 Hz. The gate voltages were applied by source meters (Keithley: Model 2400 and 2450). Devices were measured in a He-3 cryostat (Janis research) or in a variable temperature insert (Cryogenics).

Electrostatic simulation

We used COMSOL Multiphysics® to simulate the electrostatic potential in bilayer graphene.

Initial condition and boundary condition: First, we built the geometries composed of the bilayer graphene, twisted bilayer BN, (bottom thick BN), and bottom graphite in shapes of rectangular cuboids (Supplementary Fig. 9). The device lateral size was set to be 80 nm × 80 nm, and the thicknesses were assigned according to the device structures that we study. We set the moiré wavelength of twisted bilayer BN to be 18.5 nm. For the initial condition, we assume sinusoidal 2D charge density distribution on either side of the twisted bilayer BN, taking the form $\rho = 2\rho_0(\sin(kx + \sqrt{3}ky) - \sin 2kx + \sin(kx - \sqrt{3}ky))/3\sqrt{3}$, where $k = 1/a$. The peak value of charge density is taken to be $\rho_0 = \epsilon_0 \epsilon_{BN} V_p / d_B$, where ϵ_0 is the vacuum permittivity, $V_p = 0.109$ V is the interlayer potential, and d_B is the interlayer distance between bilayer BN^{23,44}. For the boundary condition, we set the bilayer graphene and bottom graphite to be grounded, i.e., chemical potential $V_0 = 0$.

Quantum capacitance treatment: Since bilayer graphene is not a perfect metal and has finite DOS, we need to consider the effect from its quantum capacitance. After the first round of simulation as described above, we acquired the electric field distribution close to the bilayer graphene, and calculated the doping induced by the electric field using Gauss's law: $n = \epsilon_0 \epsilon_{BN} E$, where ϵ_{BN} is taken to be 3. Then we calculated the chemical potential shift V_1 in bilayer graphene due to this doping effect. We then set the new boundary condition at bilayer graphene to be $V_2 = 1/2(V_0 + V_1)$, and performed the simulation again. We performed the above steps in an iterative way until the electric

potential in bilayer graphene converges, where the system reaches the electrochemical equilibrium. This means that the electrostatic potential shift due to geometric capacitance and the chemical potential shift due to quantum capacitance are both considered, and the potential profile is self-consistent. To calculate V_1 , we first acquired Fermi wavevector from $k_F = \sqrt{\pi n}$, considering the valley and spin degeneracy in bilayer graphene, and then derived V_1 from k_F using the dispersion relation calculated from Supplementary Equation 1.

Data availability

The experimental data in the study are available at Harvard Dataverse: <https://doi.org/10.7910/DVN/YJVSAK>. The DFT calculation were generated using free and open-source first-principles packages as described in Supplementary Note 9. The datasets generated during the DFT calculation are available from the corresponding author upon request.

Code availability

The COMSOL Multiphysics® file and Matlab code for electrostatic simulation are available at <https://github.com/xirui-wang/TwistedBN-Simulation>. Further simulation details are available from the corresponding author upon request. The code for band structure calculation is available at https://github.com/chengxu20/hBN_gra_moire. The code for the DFT calculation is available from the corresponding author upon request.

References

- Song, J. C. W. & Gabor, N. M. Electron quantum metamaterials in van der Waals heterostructures. *Nat. Nanotechnol.* **13**, 986–993 (2018).
- Cao, Y. et al. Correlated insulator behaviour at half-filling in magic-angle graphene superlattices. *Nature* **556**, 80–84 (2018).
- Cao, Y. et al. Unconventional superconductivity in magic-angle graphene superlattices. *Nature* **556**, 43–50 (2018).
- Sharpe, A. L. et al. Emergent ferromagnetism near three-quarters filling in twisted bilayer graphene. *Science* **365**, 605–608 (2019).
- Serlin, M. et al. Intrinsic quantized anomalous Hall effect in a moiré heterostructure. *Science* **367**, 900–903 (2020).
- Wang, L. et al. Correlated electronic phases in twisted bilayer transition metal dichalcogenides. *Nat. Mater.* **19**, 861–866 (2020).
- Li, T. et al. Quantum anomalous Hall effect from intertwined moiré bands. *Nature* **600**, 641–646 (2021).
- Cai, J. et al. Signatures of fractional quantum anomalous Hall states in twisted MoTe₂. *Nature* **622**, 63–68 (2023).
- Park, H. et al. Observation of fractionally quantized anomalous Hall effect. *Nature* **622**, 74–79 (2023).
- Xu, F. et al. Observation of Integer and Fractional Quantum Anomalous Hall Effects in Twisted Bilayer MoTe₂. *Phys. Rev. X* **13**, 031037 (2023).
- Zeng, Y. et al. Thermodynamic evidence of fractional Chern insulator in moiré MoTe₂. *Nature* **622**, 69–73 (2023).
- Dubey, S. et al. Tunable Superlattice in Graphene To Control the Number of Dirac Points. *Nano Lett.* **13**, 3990–3995 (2013).
- Drienovsky, M. et al. Towards superlattices: Lateral bipolar multi-barriers in graphene. *Phys. Rev. B* **89**, 115421 (2014).
- Forsythe, C. et al. Band structure engineering of 2D materials using patterned dielectric superlattices. *Nat. Nanotechnol.* **13**, 566–571 (2018).
- Huber, R. et al. Gate-Tunable Two-Dimensional Superlattices in Graphene. *Nano Lett.* **20**, 8046–8052 (2020).
- Li, Y. et al. Anisotropic band flattening in graphene with one-dimensional superlattices. *Nat. Nanotechnol.* **16**, 525–530 (2021).
- Barcons Ruiz, D. et al. Engineering high quality graphene superlattices via ion milled ultra-thin etching masks. *Nat. Commun.* **13**, 6926 (2022).
- Sun, J. et al. Signature of Correlated Insulator in Electric Field Controlled Superlattice. *Nano Lett.* **24**, 13600–13606 (2024).
- Zhang, Z. et al. Engineering correlated insulators in bilayer graphene with a remote Coulomb superlattice. *Nat. Mater.* **23**, 189–195 (2024).
- Gu, J. et al. Remote imprinting of moiré lattices. *Nat. Mater.* **23**, 219–223 (2024).
- He, M. et al. Dynamically tunable moiré exciton Rydberg states in a monolayer semiconductor on twisted bilayer graphene. *Nat. Mater.* **23**, 224–229 (2024).
- Woods, C. R. et al. Charge-polarized interfacial superlattices in marginally twisted hexagonal boron nitride. *Nat. Commun.* **12**, 347 (2021).
- Yasuda, K., Wang, X., Watanabe, K., Taniguchi, T. & Jarillo-Herrero, P. Stacking-engineered ferroelectricity in bilayer boron nitride. *Science* **372**, 1458–1462 (2021).
- Vizner Stern, M. et al. Interfacial ferroelectricity by van der Waals sliding. *Science* **372**, 1462–1466 (2021).
- Kim, D. S. et al. Electrostatic moiré potential from twisted hexagonal boron nitride layers. *Nat. Mater.* **23**, 65–70 (2024).
- Zhao, P., Xiao, C. & Yao, W. Universal superlattice potential for 2D materials from twisted interface inside h-BN substrate. *npj 2D Mater. Appl.* **5**, 38 (2021).
- Hunt, B. et al. Massive Dirac Fermions and Hofstadter Butterfly in a van der Waals Heterostructure. *Science* **340**, 1427–1430 (2013).
- Dean, C. R. et al. Hofstadter's butterfly and the fractal quantum Hall effect in moiré superlattices. *Nature* **497**, 598–602 (2013).
- Ponomarenko, L. A. et al. Cloning of Dirac fermions in graphene superlattices. *Nature* **497**, 594–597 (2013).
- Krishna Kumar, R. et al. High-order fractal states in graphene superlattices. *Proc. Natl Acad. Sci.* **115**, 5135–5139 (2018).
- Yankowitz, M. et al. Dynamic band-structure tuning of graphene moiré superlattices with pressure. *Nature* **557**, 404–408 (2018).
- Mao, J. et al. Evidence of flat bands and correlated states in buckled graphene superlattices. *Nature* **584**, 215–220 (2020).
- McGilly, L. J. et al. Visualization of moiré superlattices. *Nat. Nanotechnol.* **15**, 580–584 (2020).
- Kazmierczak, N. P. et al. Strain fields in twisted bilayer graphene. *Nat. Mater.* **20**, 956–963 (2021).
- Ni, G. X. et al. Soliton superlattices in twisted hexagonal boron nitride. *Nat. Commun.* **10**, 4360 (2019).
- Moore, S. L. et al. Nanoscale lattice dynamics in hexagonal boron nitride moiré superlattices. *Nat. Commun.* **12**, 5741 (2021).
- Luo, Y. et al. In situ nanoscale imaging of moiré superlattices in twisted van der Waals heterostructures. *Nat. Commun.* **11**, 4209 (2020).
- de Jong, T. A. et al. Imaging moiré deformation and dynamics in twisted bilayer graphene. *Nat. Commun.* **13**, 70 (2022).
- Li, H. et al. Imaging moiré flat bands in three-dimensional reconstructed WSe₂/WS₂ superlattices. *Nat. Mater.* **20**, 945–950 (2021).
- Magorrian, S. J. et al. Multifaceted moiré superlattice physics in twisted WSe₂ bilayers. *Phys. Rev. B* **104**, 125440 (2021).
- Zeng, Y. et al. Gate-tunable topological phases in superlattice modulated bilayer graphene. *Phys. Rev. B* **109**, 195406 (2024).
- Tan, T., Reddy, A. P., Fu, L. & Devakul, T. Designing Topology and Fractionalization in Narrow Gap Semiconductor Films via Electrostatic Engineering. *Phys. Rev. Lett.* **133**, 206601 (2024).
- Angeli, M. & MacDonald, A. H. Γ valley transition metal dichalcogenide moiré bands. *Proc. Natl Acad. Sci.* **118**, e2021826118 (2021).
- Wang, X. et al. Interfacial ferroelectricity in rhombohedral-stacked bilayer transition metal dichalcogenides. *Nat. Nanotechnol.* **17**, 367–371 (2022).
- Weston, A. et al. Interfacial ferroelectricity in marginally twisted 2D semiconductors. *Nat. Nanotechnol.* **17**, 390–395 (2022).
- Ghorashi, S. A. A. & Cano, J. Multilayer graphene with a superlattice potential. *Phys. Rev. B* **107**, 195423 (2023).
- Ghorashi, S. A. A. et al. Topological and stacked flat bands in bilayer graphene with a superlattice potential. *Phys. Rev. Lett.* **130**, 196201 (2023).

48. Suri, N., Wang, C., Hunt, B. M. & Xiao, D. Superlattice engineering of topology in massive Dirac fermions. *Phys. Rev. B* **108**, 155409 (2023).
49. Hougland, N., Ramachandran, R., Levy, J. & Pekker, D. *Theory of engineering flat bands in graphene using doubly-periodic electrostatic gating*. Preprint at <https://arxiv.org/abs/2110.15477> (2021).
50. Skuratovska, A., Tsirkin, S. S., Natterer, F. D., Neupert, T. & Fischer, M. H. Flat bands with fragile topology through superlattice engineering on single-layer graphene. *Phys. Rev. Res.* **3**, L032003 (2021).
51. Shi, L., Ma, J. & Song, J. C. W. Gate-tunable flat bands in van der Waals patterned dielectric superlattices. *2D Mater.* **7**, 015028 (2020).
52. Zhou, H. et al. Half- and quarter-metals in rhombohedral trilayer graphene. *Nature* **598**, 429–433 (2021).
53. Liu, K. et al. Spontaneous broken-symmetry insulator and metals in tetralayer rhombohedral graphene. *Nat. Nanotechnol.* **19**, 188–195 (2024).
54. Han, T. et al. Correlated insulator and Chern insulators in pentalayer rhombohedral-stacked graphene. *Nat. Nanotechnol.* <https://doi.org/10.1038/s41565-023-01520-1> (2023).
55. Dong, Z., Patri, A. S. & Senthil, T. Theory of Quantum Anomalous Hall Phases in Pentlayer Rhombohedral Graphene Moiré Structures. *Phys. Rev. Lett.* **133**, 206502 (2024).
56. Dong, J. et al. Anomalous Hall Crystals in Rhombohedral Multilayer Graphene. I. Interaction-Driven Chern Bands and Fractional Quantum Hall States at Zero Magnetic Field. *Phys. Rev. Lett.* **133**, 206503 (2024).
57. Zhou, B., Yang, H. & Zhang, Y.-H. Fractional Quantum Anomalous Hall Effect in Rhombohedral Multilayer Graphene in the Moiréless Limit. *Phys. Rev. Lett.* **133**, 206504 (2024).
58. Tan, T. & Devakul, T. Parent Berry Curvature and the Ideal Anomalous Hall Crystal. *Phys. Rev. X* **14**, 041040 (2024).
59. Tan, T., May-Mann, J. & Devakul, T. *Wavefunction approach to the fractional anomalous Hall crystal*. Preprint at <https://doi.org/10.48550/arXiv.2409.06775> (2024).
60. Barthelemy, P. & Vandersypen, L. M. K. Quantum Dot Systems: a versatile platform for quantum simulations. *Ann. Phys.* **525**, 808–826 (2013).
61. Hensgens, T. et al. Quantum simulation of a Fermi–Hubbard model using a semiconductor quantum dot array. *Nature* **548**, 70–73 (2017).
62. Freeney, S. E., Slot, M. R., Gardenier, T. S., Swart, I. & Vanmaekelbergh, D. Electronic Quantum Materials Simulated with Artificial Model Lattices. *ACS Nanosci. Au* **2**, 198–224 (2022).
63. Kim, K. et al. van der Waals heterostructures with high accuracy rotational alignment. *Nano Lett.* **16**, 1989–1995 (2016).
64. Cao, Y. et al. Superlattice-Induced Insulating States and Valley-Protected Orbits in Twisted Bilayer Graphene. *Phys. Rev. Lett.* **117**, 116804 (2016).
65. Izumi, F. et al. VESTA 3 for three-dimensional visualization of crystal, volumetric and morphology data. *J. Appl. Crystallogr.* **44**, 1272–1276 (2011).

Acknowledgements

We thank A. Reddy for help in fabrication, and J. Cano, S.A.A. Ghorashi, M. Koshino, and V.I. Fal'ko for fruitful discussions. This research was supported by the Center for the Advancement of Topological Semimetals, an Energy Frontier Research Center funded by the U.S. Department of Energy Office of Science, through the Ames Laboratory under contract DE-AC02-07CH11358 (measurements and data analysis), the MIT/Microsystems Technology Laboratories Samsung Semiconductor Research Fund, the Gordon and Betty Moore Foundation's EPIQS Initiative through grant GBMF9463, and the Ramon Areces Foundation. This work was performed in part at the Harvard University Center for Nanoscale Systems (CNS), a member of the National Nanotechnology

Coordinated Infrastructure Network (NNCI), which is supported by the National Science Foundation under NSF ECCS award No. 1541959. This work was carried out in part through the use of MIT.nano's facilities. C.X. and Y.Z. are supported by the start-up fund at University of Tennessee Knoxville, and the Max Planck Partner lab on quantum materials from Max Planck Institute Chemical Physics of Solids. S.A. is partially supported by the NSF Graduate Research Fellowship Program via grant no. 1122374. D.B. and E.K. acknowledge the US Army Research Office (ARO) MURI project under grant No. W911NF-21-0147 and from the Simons Foundation award No. 896626. N.P. acknowledges the Kavli Institute for Theoretical Physics (KITP) graduate fellowship. K.W. and T.T. acknowledge support from the JSPS KAKENHI (Grant Numbers 21H05233 and 23H02052) and World Premier International Research Center Initiative (WPI), MEXT, Japan.

Author contributions

K.Y., X.W., and P.J.-H. conceived the project and experiments. K.Y., X.W., and S.A. fabricated the devices and performed measurements with the help of C.C.; X.W. performed electrostatic simulations with Comsol Multiphysics®. Y.Z., C.X., D.B., N.P., and P.J.D.C. performed the theoretical calculations. K.W. and T.T. grew the BN crystals. K.Y., P.J.-H., Y.Z., E.K., and R.A. supervised the project. X.W. and K.Y. analyzed the data and wrote the manuscript with input from all the other authors.

Competing interests

The authors declare no competing interests.

Additional information

Supplementary information The online version contains supplementary material available at <https://doi.org/10.1038/s41467-024-55432-2>.

Correspondence and requests for materials should be addressed to Pablo Jarillo-Herrero or Kenji Yasuda.

Peer review information *Nature Communications* thanks Jianming Lu, and the other, anonymous, reviewer(s) for their contribution to the peer review of this work. A peer review file is available.

Reprints and permissions information is available at <http://www.nature.com/reprints>

Publisher's note Springer Nature remains neutral with regard to jurisdictional claims in published maps and institutional affiliations.

Open Access This article is licensed under a Creative Commons Attribution-NonCommercial-NoDerivatives 4.0 International License, which permits any non-commercial use, sharing, distribution and reproduction in any medium or format, as long as you give appropriate credit to the original author(s) and the source, provide a link to the Creative Commons licence, and indicate if you modified the licensed material. You do not have permission under this licence to share adapted material derived from this article or parts of it. The images or other third party material in this article are included in the article's Creative Commons licence, unless indicated otherwise in a credit line to the material. If material is not included in the article's Creative Commons licence and your intended use is not permitted by statutory regulation or exceeds the permitted use, you will need to obtain permission directly from the copyright holder. To view a copy of this licence, visit <http://creativecommons.org/licenses/by-nc-nd/4.0/>.

© The Author(s) 2024